JACS
JOURNAL OF THE AMERICAN CHEMICAL SOCIETY
pubs.acs.org/JACS
Article

Charge Separation and/or Hot Spots: Clarification of Efficient CO_2 Reduction over Ru−Ni Nanoparticles Compared to Photocatalysis on Ru−Ni−ZrO_2 Composites

Masahito Sasaki, Tomoki Oyumi, Keisuke Hara, Hongwei Zhang,* and Yasuo Izumi*

Cite This: https://doi.org/10.1021/jacs.5c17533
Read Online
ACCESS | Metrics & More | Article Recommendations | Supporting Information

ABSTRACT: The true reaction pathway and the catalytic role responsible for it remain uncertain in photocatalysis, where charge separation, hot spots, and energetic modulation of the ground and excited states are involved. Herein, a Ru atom was embedded in a ∼1.6 nm Ni nanoparticle dispersed on ZrO_2. The $^{13}CO_2$ photoreduction rate to $^{13}CH_4$ showed a negligible change of ∼26 μmol h^{-1} g_{cat}^{-1} upon adding Ru (1.0 wt %) to the Ni (10 wt %)-ZrO_2 photocatalyst under a 295 K water bath for cooling irradiated by UV−visible light at 568 mW cm^{-2}. By contrast, the rate using the Ru−Ni−ZrO_2 catalyst exceeded that of Ni−ZrO_2 by >2.7× (>7.9 mmol h^{-1} g_{cat}^{-1}) when the 295 K water bath for catalysts was not applied. Extended X-ray absorption fine structure analysis revealed that the hot spot Ni temperature increased from 295 to 399 ± 29 K under 654 mW cm^{-2} irradiation, even with the 295 K ethylene glycol bath for cooling, confirming that multiple hydrogenations occurred on Ni for COH species transferred from the O vacancy sites at the ZrO_2 surface. In the absence of the 295 K water bath, CO_2 was directly adsorbed on the $RuNi_2$ site, and its dissociation into CO and O species proceeded with a low activation energy of 0.45 eV, enabling a photothermal pathway, as supported by DFT and FTIR analyses. These results highlight the importance of monitoring the hot spot temperature in photocatalysts to identify the active site combined with redox sites on the semiconductor, driven by charge separation under UV−visible light irradiation.

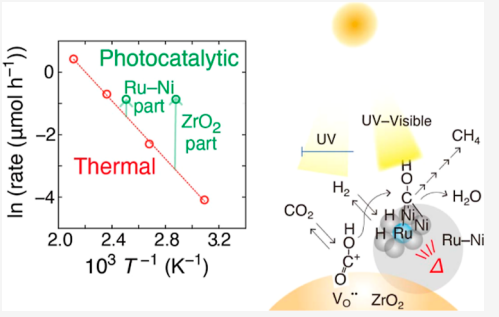

1. INTRODUCTION

Photocatalytic reduction of CO_2 has been extensively investigated as a promising approach to establishing a carbon−neutral cycle in a sustainable society.[1,2] The most critical challenge for the photocatalytic reduction of CO_2 is its low efficiency in converting CO_2 into fuels[3−5] and/or valuable chemicals.[4,5] To overcome this problem, strategies to increase charge separation efficiency and dramatically enhance photocatalytic activity—such as increasing the irradiation light intensity on semiconductor-based photocatalysts—need to be explored.

Historically, Ru has presented a puzzling case in catalytic CO_2 reduction. Under UV−visible light irradiation, CO_2 was reduced to CH_4 using Ru−TiO_2,[6,7] primarily owing to heat generated from light energy, while the contribution of charge separation leading to redox reactions at the catalyst surface was negligible, as evidenced by comparisons with catalytic reaction rates driven by external heating under dark conditions.[7]

Recently, the effects of single Ru have been reported to lower the activation energy (E_{act}) of the rate-determining step in thermal CO_2 hydrogenation, mostly during CO_2 adsorption or CO hydrogenation.[8,9] By contrast, in photocatalytic CO_2 hydrogenation, single Ru embedded on Cu nanoparticles supported on $Bi_4Ti_3O_{12}$ enhanced CO_2 adsorption and its subsequent conversion into OCOH species.[10] Recently, Ozin, Yao, and colleagues reported micro- and nanoscale thermometry to probe the temperature of the catalyst in photothermal reactors, highlighting the difficulty of distinguishing photothermal effects from surplus catalytic activity arising from light-induced heating.[11] One plausible pathway of photothermal excitation of reactant is the vibrational excitation of the reactant by light, which facilitates their transformation to products.[11] In a related study, the dependence of CO_2 hydrogenation rates on irradiated UV−visible light intensity was investigated using an Fe−ZrO_2 catalyst, revealing a two-step reaction mechanism: an initial redox reaction driven by charge separation in ZrO_2, followed by multiple hydrogenation steps on the Fe^0 surface.[5] As the irradiated light intensity increased from 110 to 472 mW cm^{-2}, the contribution of charge separation in ZrO_2 became negligible to the overall pathway from CO_2 to CH_4, which occurred primarily on the Fe^0 surface owing to heat generated from light. Thus, the origin of catalysis—whether thermal, photothermal, and/or

Received: October 6, 2025
Revised: March 8, 2026
Accepted: March 12, 2026

photocatalytic—often remains elusive, making the reaction mechanism unclear in semiconductor-based (photo)catalysts.

Herein, reaction pathways from CO_2 to CH_4 were clarified using a Ru−Ni−ZrO_2 catalyst under the irradiation of UV−visible light, whether photocatalytic or photothermal, by controlling the catalyst temperature with or without a 295 K bath, as well as varying the UV−visible light intensity between 90 and 900 mW cm^{-2}. Under irradiation at 568 mW cm^{-2}, the Ru atom embedded in the Ni nanoparticle remarkably accelerated $^{13}CH_4$ formation from $^{13}CO_2$, reaching one of the highest rates to date. This enhancement was attributed to CO_2 adsorption on the Ru site and its subsequent dissociation into CO and O species, as confirmed by extended X-ray absorption fine structure (EXAFS), FTIR spectroscopy, and density functional theory (DFT) calculations. By contrast, the photocatalytic pathway proceeded via OCO + H to OCOH species at the O vacancy ($V_O^{\bullet\bullet}$) site on the semiconductor ZrO_2 surface, driven by charge separation under UV light (Supporting Information, Section 3.1),[3−5,12,13] followed by transfer of COH species and multiple hydrogenation steps over the hot spot Ni. This pathway from COH to CH_4 was primarily driven by heat generated from the light energy at 568−654 mW cm^{-2} under a 295 K bath.

2. EXPERIMENTAL METHODS

2.1. Catalyst Preparation

To prepare the composite catalysts comprising Ni, Ru, and ZrO_2, the concentration of Ni was fixed at 10 wt %, while the Ru loading was varied between 0.5 and 2.0 wt % in the final composites. In a typical procedure, ZrO_2 (0.445 g; Type JRC-ZRO-3, Catalysis Society of Japan; predominantly monoclinic with a minor tetragonal phase; specific surface area = 94.4 m^2 g^{-1}) was dispersed in deionized water (200 mL; <0.055 μS cm^{-1}). The suspension was ultrasonicated (360 W, 40 kHz) for 20 min and magnetically stirred at 1000 rotations per minute (rpm) for 1 h. Next, Ni(II) chloride hexahydrate (0.2025 g; Macklin Biochemical Technology, Shanghai, China) and Ru(III) chloride anhydrate (0.0051−0.0207 g; Macklin Biochemical Technology) were simultaneously added to the suspension and magnetically stirred at 1000 rpm for 1 h. Then, an aqueous $NaBH_4$ solution (10 mL; 0.2803−0.3027 g; Sinopharm Chemical Reagent, Shanghai, China) was added dropwise to the suspension, and the mixture was stirred at 1000 rpm for 5 min. The obtained precipitate was filtered using a poly(tetrafluoroethylene)-based membrane filter (Omnipore, Type JVWP04700, Merck−Millipore, Darmstadt, Germany; pore size = 0.1 μm) and washed with deionized water (50 mL each, 5×). The obtained samples were denoted as Ru (x wt %)−Ni (10 wt %)−ZrO_2, where x = 0.5−2.0. Following a similar procedure, Ni (10 wt %)−ZrO_2 and Ru (1.0 wt %)−ZrO_2 samples were prepared as reference catalysts using $NiCl_2{\cdot}6H_2O$ or $RuCl_3$.

2.2. Catalytic Reduction Tests of CO_2 under Light

CO_2 reduction tests using H_2 were conducted using 20 mg of catalysts. The catalyst powder was placed in a U-shaped quartz reactor connected to a Pyrex glass circulation system (206.1 mL) and evacuated under a vacuum (10^{-6} Pa) for 1 h. Subsequently, the catalyst was exposed to H_2 (purity >99.99%; 21.7 kPa), heated to 723 K at a ramp rate of 15 K min^{-1}, and maintained at 723 K for 10 min, followed by evacuation and cooling to 295 K. The reduced catalyst is denoted, for example, as Ru−Ni−ZrO_2-723R (Reduction).

Then, catalytic tests for $^{13}CO_2$ reduction were performed using the reduced catalysts, $^{13}CO_2$ (2.3 kPa; ^{13}C 99.0%, ^{17}O 0.1%, purity >99.9%, Cambridge Isotope Laboratories, Inc., Tewksbury, MA), H_2 (21.7 kPa), and UV−visible light irradiation from a 300 W Xe arc lamp (Model MAX-350, Asahi Spectrum, Japan). The wavelength dependence of light intensity and the corresponding absorbance by photocatalysts are depicted in Figures S1 and S4, respectively. $^{13}CO_2$ was used to kinetically monitor the reaction pathway also in the FTIR study (see Section 2.3). The distance between the quartz light guide exit of the UV−visible light source (Φ = 5.0 mm) and the catalyst was kept at 1 cm for all tests. Light intensity was measured by using a photosensor (Model PCM-01, Prede, Tokyo, Japan) and a counter (Model KADEC-UP, North One, Sapporo, Japan) and recorded for each test. Experiments were conducted both with cooling the reactor via a water bath (2.5 L, Chart S1) and without a water bath, while both were irradiated with UV−visible light.

During $^{13}CO_2$ photoreduction tests, a packed column of 13X-S molecular sieves (3 m length, 3 mm internal diameter; GL Sciences, Inc., Japan) was used for online gas chromatography−mass spectrometry analyses (Model JMS-Q1050GC, JEOL, Tokyo, Japan) with helium (0.40 MPa, purity >99.9999%) as the carrier gas. ^{13}CO (mass-to-charge ratio (m/z) = 29 for $^{13}CO^+$), $^{13}CH_4$ (m/z = 17 for $^{13}CH_4^+$), $^{12}CH_4$ (m/z = 16 for $^{12}CH_4^+$), and $^{13}C_2H_6$ (m/z = 30 for $^{13}C_2H_4^+$) were well separated and evaluated in each mass chromatogram. $^{13}CH_4$ and $^{12}CH_4$ were quantified based on their m/z of 17 and 16, respectively, considering the fragment ratio of CH_3^+/CH_4^+ (0.708:1).

2.3. Characterizations

Ni and Ru K-edge XAFS spectra were measured in the transmission mode on beamline 9C at the Photon Factory and on beamline NW10A at the Photon Factory Advanced Ring, respectively, at the High Energy Accelerator Research Organization (Tsukuba, Japan). The Ru (1.0 wt %)−Ni (10 wt %)−ZrO_2 sample powder (120 mg) was prepared in a Pyrex glass U-tube connected to a quartz XAFS cell (sample diameter Φ = 20 mm, thickness t = 1 mm). The sample in the U-tube was reduced under H_2 at 723 K, then evacuated, and filled with CO_2 (2.3 kPa) and H_2 (21.7 kPa). The powder was subsequently transferred from the U-tube to the XAFS cell, which remained connected to the U-tube. The samples did not contact air throughout the experiments. The XAFS cell was equipped with polyethylene terephthalate (PET) film windows (Toyobo Film Solutions, Japan, G200X-38; t = 38 μm) to allow both UV−visible light and X-ray transmission. Then, the XAFS cell was immersed in an ethylene glycol (EG) bath at 295 K (Chart S2), which minimized bubble formation in the X-ray beam path during time-resolved monitoring at both the Ni and Ru K-edges. The sample was then irradiated with UV−visible light from a Xe arc lamp (Model MAX-350) at the beamline. X-rays were transmitted perpendicularly through the disk, whereas UV−visible light was incident at 45° relative to the X-ray direction. The distance between the light exit of the quartz fiber light guide and the sample was 5 cm. The light intensity at the sample position was 654 mW cm^{-2}. The monitoring without an EG bath was difficult because the PET windows melted during monitoring.

At beamline 9C, the storage ring energy was 2.5 GeV with a ring current of 450 mA. At beamline NW10A, the storage ring energy was 6.5 GeV with a ring current of 50 mA. A Si(1 1 1) double-crystal monochromator and a Si(3 1 1) double-crystal monochromator, along with Rh- and Pt-coated focusing bent cylindrical mirrors, were inserted into the X-ray beam paths at 9C and NW10A, respectively. At both beamlines, a piezo transducer was used to detune the X-ray intensity to two-thirds of the maximum to suppress high harmonics compared to primary X-rays. The Ni and Ru K-edge absorption energies were calibrated at 8331.65 and 22,119.3 eV, respectively, using spectra of Ni metal foil (5.0 μm thick) and Ru metal powder.[14] The obtained Ni and Ru K-edge XAFS data were analyzed using XDAP software, version 3.2.9.[15] The empirical amplitude of oscillation was extracted from the EXAFS data for Ni and Ru metals as well as NiO and RuO_2 powders. For Ni metal (lattice constant a = 0.35238 nm), the interatomic distance (R) for the Ni−Ni pair was set to 0.24917 nm with a coordination number (N) of 12.[16] For NiO (a = 0.4176 nm), the R values for the Ni−O and Ni−Ni pairs were set to 0.2088 nm with an N value of 6 and to 0.2953 nm with an N value of 12, respectively.[17] For Ru metal (lattice constants a = 0.27059 nm, c = 0.42815 nm), the R value for the Ru−Ru pair was set to 0.26780 nm with an N value of 12.[16] We assumed that the many-body reduction factors were identical for both the sample and the reference.

https://doi.org/10.1021/jacs.5c17533
J. Am. Chem. Soc. XXXX, XXX, XXX−XXX

The temperatures of local Ni and Ru sites were monitored using the Debye−Waller factor obtained from curve-fitting analysis in XDAP and the correlated Debye model.[18,19] EXAFS analysis indicated that Ru atoms substituted for Ni atoms at the Ni metal surface, which was further supported by structural optimization using DFT calculations (see Section 3.4., photocatalytic CO_2 reduction pathway). The correlation between site temperature and the Debye−Waller factor was calculated for both Ni and Ru sites (Figure S2A,B, respectively) based on the Debye temperature for Ni (bulk 450 K;[20] surface perpendicular translational motion ⊥: 208 K; surface parallel translational motion ∥: 348 K[21]) using FEFF version 8.40.[22] Calculations for Ru were performed using the Debye temperature for Ni because the Ru atom was embedded in the Ni crystal (see Section 3.2., Ni and Ru Site Structure and Temperature Analyses via XAFS; Table S1).

In situ FTIR spectroscopy measurements were performed at 295 K over a range of 4000−650 cm^{-1} using a Model FT/IR-4200 instrument (JASCO, Tokyo, Japan). Ru (1.0 wt %)−Ni (10 wt %)−ZrO_2 and Ni (10 wt %)−ZrO_2 catalyst disks (71 mg each, Φ = 2 cm) were heated under H_2 at 723 K in a quartz cell and then transferred to a quartz FTIR cell inside a glovebox (UN-6509LCIY, Unico, Japan). The sample disks were irradiated with UV−visible light from a Xe arc lamp (Model MAX-350) through a quartz fiber light guide. The distance between the fiber light exit and the sample disk was 5 cm, and the light intensity was controlled between 90 and 900 mW cm^{-2}. The energy resolution of the spectrometer was set to 1 cm^{-1}, and data were accumulated over 512 scans (~2 s per scan).

2.4. DFT Calculations

Spin-polarized periodic DFT calculations were conducted using the Vienna Ab initio Simulation Package version 6.4.2[23] on a WJ9J-W231 Server comprising an Intel Xeon w9-3495X processor (1.9 GHz, 56 cores; Tsukumo, Japan) and a VT64 Server XS2-2TI comprising four units of Intel Xeon Platinum 9242 processors (2.3 GHz, 48 cores; Visual Technology, Tokyo, Japan). Additional computations were performed using the supercomputer facilities at the Institute for Solid State Physics, University of Tokyo, Japan. The projector-augmented wave method was employed at the DFT-D3 level to account for van der Waals interactions. The generalized gradient approximation (GGA) with the revised Perdew−Burke−Ernzerhof (RPBE) exchange−correlation functional was employed by setting a plane-wave energy cutoff of 500 eV. Each optimized structure was obtained at the D3 level employing the GGA−RPBE functional and adding a Hubbard U parameter (4.0 eV) for Zr.[24,25]

The convergence criterion was set to 10^{-4} eV for the self-consistent field cycle, and optimizations were considered converged when the forces on all atoms were smaller than 0.1 eV $Å^{-1}$ (Å = 0.1 nm), which was small enough based on convergence tests (Table S3). All of the atoms were fully relaxed during structural optimization. The Brillouin zone was sampled with a 3 × 3 × 1 wavenumber vector k-point grid. Transition states were pursued using the climbing-image nudged elastic band (CI-NEB) method.[26]

The (1 1 1) surface of face-centered cubic (fcc) Ni, modeled with (2 × 2 × 2) element unit cells, was chosen as the slab model, with a vacuum spacing of 1.0 nm between slabs.[27] Separately, a hemispherical Ni_{19} cluster exposing the (1 1 1) face, based on the fcc structure, and a Ni metal cluster in which one Ni atom was replaced by a Ru atom ($RuNi_{18}$) were combined with a monoclinic ZrO_2(1 1 1) surface.[27]

The adsorption energy (E_{ads}) of the adsorbate was calculated based on eq 1

$$E_{ads} = E_{mol/slab} - E_{mol} - E_{slab} \quad (1)$$

where $E_{mol/slab}$, E_{mol}, and E_{slab} are the total energies of the adsorbate on the slab model, the isolated molecule in the gas phase, and the bare surface, respectively.

3. RESULTS AND DISCUSSION

3.1. CO_2 Reduction Tests Irradiated under UV−Visible Light

Preliminary CO_2 photoreduction tests were performed under CO_2 (10 kPa), H_2 (50 kPa), and UV−visible light irradiation (620 mW cm^{-2} at the photocatalyst) using Ru (0 wt %−2.0 wt %)−Ni (10 wt %)−ZrO_2 photocatalysts (Table S2). The CH_4 formation rate reached a maximum when the Ru content was 1.0 wt % (entry c). Therefore, the Ru (1.0 wt %)−Ni (10 wt %)−ZrO_2 photocatalyst was chosen for subsequent photocatalytic tests and characterization. Furthermore, the CH_4 formation rates were proportional to the square of the irradiated UV−visible light intensity using the catalysts, consistent with our previous study results.[3]

$^{13}CO_2$ photoreduction tests were performed using isotopically labeled $^{13}CO_2$ (2.3 kPa) and H_2 (21.7 kPa) with the Ru (1.0 wt %)−Ni (10 wt %)−ZrO_2 photocatalyst under the irradiation of UV−visible light (568 mW cm^{-2} at the photocatalyst). The photoreactor was maintained in a water bath at 295 K (Figure 1 and Chart S1) to suppress thermal

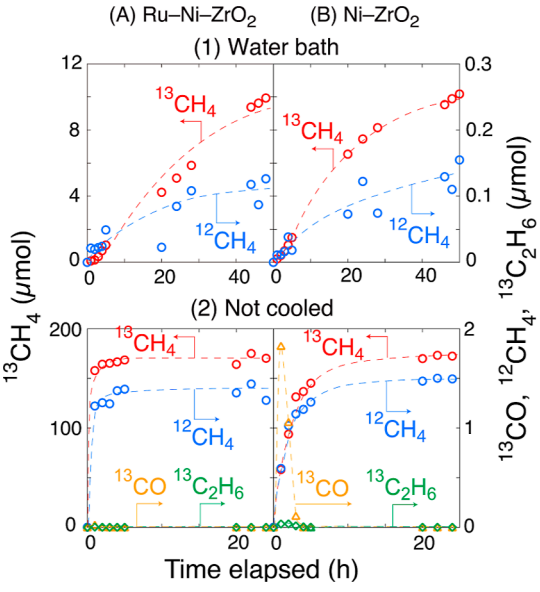

Figure 1. Time course of ^{13}CO, $^{13}CH_4$, $^{12}CH_4$, and $^{13}C_2H_6$ formation under $^{13}CO_2$ (2.3 kPa) and H_2 (21.7 kPa) using Ru (1.0 wt %)−Ni (10 wt %)−ZrO_2 (A) and Ni (10 wt %)−ZrO_2 (B) catalysts. Reactions were performed under UV−visible light irradiation at 568 mW cm^{-2} at the catalyst position with the photoreactor maintained in a 295 K bath (1) and 568 mW cm^{-2} at the catalyst position without the bath (2).

reactions arising from light-to-heat conversion, and the results were compared with those obtained using Ni (10 wt %)−ZrO_2 photocatalyst (Figure 1). For both photocatalysts, the major product was $^{13}CH_4$, and the $^{13}CH_4$ formation rate using Ru−Ni−ZrO_2 (21 μmol h^{-1} g_{cat}^{-1}) was equivalent or slightly inferior to that observed with Ni−ZrO_2 (26 μmol h^{-1} g_{cat}^{-1}).

The molar fraction of $^{12}CH_4$ in total CH_4 formation $\left(\frac{12CH_4}{12CH_4 + 13CH_4}\right)$ was also very similar for both catalysts (5.0 mol %−5.2 mol %), corresponding to the ratio of $^{12}CO_2$ adsorbed from air at $V_O^{\bullet\bullet}$ sites on the ZrO_2 surface relative to the introduced $^{13}CO_2$ gas (isotopic purity 99.0%) used as the reactant.[3−5,12,13,27] These results indicate that the 1.0 wt % Ru

https://doi.org/10.1021/jacs.5c17533
J. Am. Chem. Soc. XXXX, XXX, XXX−XXX

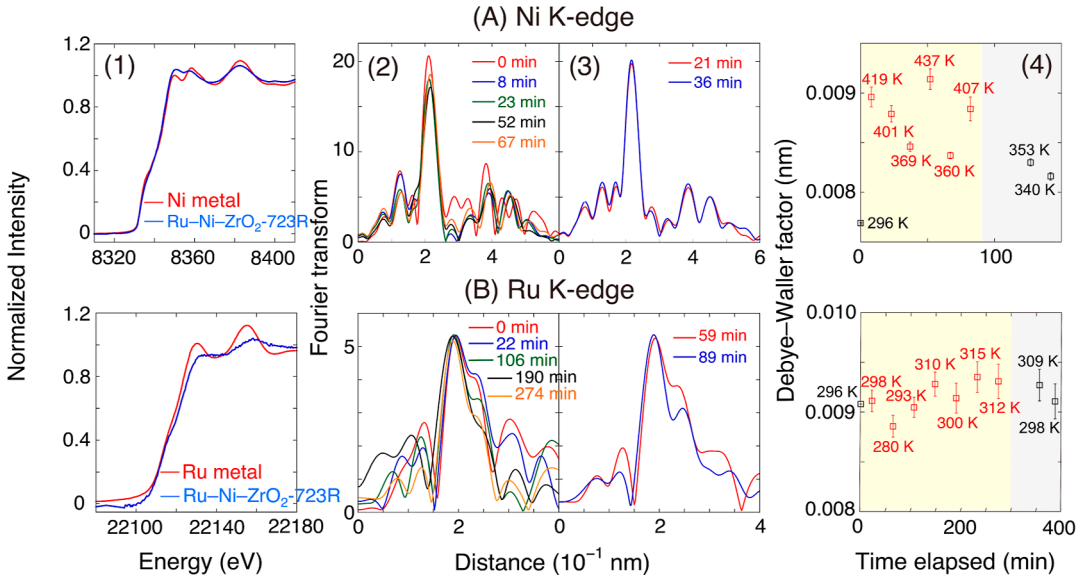

Figure 2. XAFS results at the Ni (A) and Ru K-edges (B) for Ru (1.0 wt %)−Ni (10 wt %)−ZrO_2-723R under the 295 K ethylene glycol bath using CO_2 (2.3 kPa), H_2 (21.7 kPa), and the UV−visible light irradiation (654 mW cm^{-2}). (1) Normalized X-ray absorption near-edge structure (XANES) spectra compared with the corresponding metal references; (2, 3) Fourier transform of k^3-weighted EXAFS under UV−visible light illumination (2) and after turning the light off (3); (4) Time course of the Debye−Waller factor σ for the Ni−Ni (A) and Ru−Ni (B) interatomic pairs, with the corresponding site temperatures evaluated using the correlated Debye model.

in the photocatalyst had no effects on either the $^{13}CH_4$ formation rate or the $^{12}CH_4$ fraction under $^{13}CO_2$ photoreduction in the 295 K water bath.

The photocatalytic test results under the 295 K bath (Figure 1B(1)) were compared with photocatalytic tests performed under similar UV−visible light intensity (568 mW cm^{-2}) in the absence of the 295 K bath (panels A(2) and B(2)). Under both reaction conditions, $^{13}CH_4$ was the major product for both Ru (1.0 wt %)−Ni (10 wt %)−ZrO_2 and Ni (10 wt %)−ZrO_2 photocatalysts. However, 1.0 wt % Ru acted as an effective promoter under the no-bath condition, in clear contrast to the photocatalytic results under the 295 K bath. In the absence of the 295 K bath, 2.3 kPa of $^{13}CO_2$ was completely converted within 1 h of UV−visible light irradiation, corresponding to a $^{13}CH_4$ formation rate of >7.9 mmol h^{-1} g_{cat}^{-1} for Ru (1.0 wt %)−Ni (10 wt %)−ZrO_2 (Figure 1A(2)), which is >2.7× higher than the rate of 2.9 mmol h^{-1} g_{cat}^{-1} observed with Ni (10 wt %)−ZrO_2 (panel B(2)). These results suggest that the CO_2 reduction pathway differs depending on whether the reaction is conducted under the 295 K bath or without the bath, both under UV−visible light irradiation. The catalytic test result with an empty bath (Figure S3) was essentially the same as that in Figure 1A(2).

The molar fraction of $^{12}CH_4$ in total CH_4 formation $\left(\frac{^{12}CH_4}{^{12}CH_4 + {}^{13}CH_4}\right)$ was essentially constant at 0.8 mol %−1.0 mol %, independent of the catalyst used without the bath, significantly smaller than the total amount (1.3 mol %) of the $^{12}CO_2$ impurity in the $^{13}CO_2$ reagent and $^{12}CO_2$ adsorbed on $V_O^{\bullet\bullet}$ sites from air (Supporting Information, Section 3.2), demonstrating that $^{12}CO_2$ on $V_O^{\bullet\bullet}$ sites at ZrO_2 surface was not included in the reaction pathway to CH_4, in clear contrast to these values of 5.0%−5.2% observed during tests conducted under the 295 K bath in which the contribution of $^{12}CO_2$ on $V_O^{\bullet\bullet}$ sites at ZrO_2 surface was suggested.

The $^{13}CH_4$ formation rates using the Ru (1.0 wt %)−Ni (10 wt %)−ZrO_2 catalyst differed by >380× between the presence and absence of the 295 K bath (Figure 1(2)). UV light of energy greater than the bandgap (5.0 eV) of ZrO_2 was clearly irradiated under the kinetic reaction conditions as well as a minor interband impurity level contribution, e.g., $V_O^{\bullet\bullet}$ sites, for UV absorption (Section 3.1), strongly suggesting the photocatalytic steps in the presence of a 295 K bath.[3−5,12,13,27] The reason for the dramatic difference above is elucidated below in terms of distinct reaction pathways.

3.2. Ni and Ru Site Structure and Temperature Analyses via XAFS

The Ni and Ru sites in Ru (1.0 wt %)−Ni (10 wt %)−ZrO_2-723R were analyzed using XAFS spectroscopy. X-ray absorption near-edge structure (XANES) spectra at both Ni and Ru K-edges for the Ru−Ni−ZrO_2-723R catalyst before photocatalytic testing resembled those of the corresponding metals (Figure 2A(1),B(1)). However, the postedge oscillations became weaker compared to bulk metals, reflecting the lower probability of multiple scattering of photoelectrons in the Ru−Ni nanoparticles.

Next, Ni K-edge EXAFS for Ru (1.0 wt %)−Ni (10 wt %)−ZrO_2-723R under the 295 K bath was monitored in the presence of CO_2, H_2, and UV−visible light irradiation (654 mW cm^{-2}). In the Fourier transform, the peak intensity at 0.21 nm (phase shift uncorrected) quickly decreased when the UV−visible light was turned on (Figure 2) and remained essentially constant during 90 min of light irradiation. By contrast, as soon as the UV−visible light was turned off, the peak rapidly increased, returning almost to its preirradiation intensity (Figure 2A(3)).

These changes in peak intensity during UV−visible light-on and light-off periods were attributable to the corresponding increase and decrease in the Debye−Waller factor (σ) because the associated N and R values remained essentially unchanged (Figure S9). The σ_{sample}^2 value was calculated as the summation of $\sigma_{correlated\ Debye}^2$ (for standard metal crystal, Figure S2), σ_{XDAP}^2 (from curve-fit analysis of experimental data), and

https://doi.org/10.1021/jacs.5c17533
J. Am. Chem. Soc. XXXX, XXX, XXX−XXX

$\sigma_{\text{structural disorder}}^2$ (representing plausible contribution from metal nanoparticles in the photocatalysts)

$$\sigma_{\text{sample}}^2 = \sigma_{\text{correlated Debye}}^2 + \sigma_{\text{XDAP}}^2 + \sigma_{\text{structural disorder}}^2 \quad (2)$$

The values of $\sigma_{\text{correlated Debye}}^2$, σ_{XDAP}^2, and $\sigma_{\text{structural disorder}}^2$ were determined to be 4.91×10^{-5}, -1.03×10^{-5}, and 2.10×10^{-5} nm,^{2} respectively, resulting in a σ_{sample} value of 0.00773 nm for the Ni sites (Figure 2A(4)) before UV−visible light irradiation. This calculation assumes 67% dispersion of spherical nanoparticles, corresponding to a mean particle size of 1.6 nm based on the given N value[28] and surface exposure of the hemisphere on ZrO_2 in the Ru (1.0 wt %)−Ni (10 wt %)−ZrO_2-723R photocatalyst.

By contrast, for the Ru sites, the values of $\sigma_{\text{correlated Debye}}^2$, σ_{XDAP}^2, and $\sigma_{\text{structural disorder}}^2$ were determined to be 3.97×10^{-5}, 4.22×10^{-5}, and 5.63×10^{-7} nm,^{2} respectively, providing a σ_{sample} value of 0.00908 nm (Figure 2B(4)) before UV−visible light irradiation, assuming complete surface dispersion of Ru atoms on the Ni nanoparticle.

Based on the correlation between Ni site temperature and the Debye−Waller factor for bulk and surface sites (horizontal and vertical translational motions; Figure S2(A)) in the Ni lattice, the σ value for Ni, which corresponded to 296 K before light irradiation, increased to 399 ± 29 K under UV−visible light for 90 min (Figure 2A(4)). It gradually decreased to the temperature in the beamline hutch after the light was turned off. As inner electron excitation (10^{-17}−10^{-18} s)[29] is faster than charge separation in semiconductors under light (~fs),[30] only temperature change would affect the Debye−Waller factor by the light irradiation. The PET window used for EXAFS cell cuts the UV light of λ < 320 nm, but the effects seem insignificant because Ru−Ni or Ni nanoparticles absorb the whole range of th spectrum in the UV and visible light regions (Supporting Information, Section 3.1).

Similarly, the correlation between Ru site temperature and Debye−Waller factor for bulk and surface sites (horizontal and vertical motions; Figure S2(B)) in the Ni lattice was calculated based on a single Ru atom substitution at the surface of the Ni lattice using Debye temperature values for Ni (Table S1d).[20,21]

By contrast, at the Ru K-edge, the σ value corresponding to 296 K before light irradiation changed negligibly, reaching 302 ± 12 K under UV−visible light irradiation for 300 min (Figure 2B(4)). After the light was turned off, the temperature remained constant at 304 ± 8 K. As the single Ru atom is embedded at the Ni nanoparticle surface (Scheme S2a) and is coordinated exclusively to the surrounding Ni atoms, the surface Debye temperature for Ni (vertical motion, 208 K) was used. This trend was well reproduced under similar conditions (Figure S10), and even if the corresponding Debye temperature for Ru (295 K; Table S1e) was used in the correlated Debye model, the Ru site temperature still showed a negligible change.

Based on Ru K-edge XANES (Figure 2B(1)) and the mean Ru−Ni interatomic distance of 0.240 nm (Figure S9B) for Ru (1.0 wt %)−Ni (10 wt %)−ZrO_2-723R, shorter than the Ru−Ru interatomic distance of 0.26780 nm for Ru metal and even the Ni−Ni interatomic distance of 0.24917 nm,[16] the possibilities of oxidized Ru and pure Ru nanoclusters are neglected. The Ru−Ni coordination number of 4.1 (Figure S9B) suggested an abnormally confined Ru atom in the surface layer of the Ni nanocrystal. Experimentally, σ values for confined Ru sites were greater by 0.0027−0.0035 nm compared to normal Ru metal[10,31] and theoretically, Debye temperature decreased for subnm metal nanoparticle,[32,33] in accord with greater σ value for confined Ru in this study (Figure 2A4,B4). Therefore, the correlated Debye model would not precisely monitor further increase of σ value under UV−visible light irradiation for such an abnormally confined and/or undercoordinated site (see Section S5).

In contrast, Zr K-edge EXAFS monitoring for the Ni−ZrO_2 sample showed a minor temperature increase to 323 ± 6 K @ 142 mW cm^{-2} (Figure S11) or increase to 347 K @670 mW cm^{-2} for ZrO_2 sample by IR camera (Figure S12A).

Similar monitoring of local nanoparticle metal site temperatures has been reported at Fe, Co, Ni, and Ag K-edge[3−5,12] and Au L_3-edge,[13] demonstrating site warming up to 317−459 K (Table S1) in the absence of the 295 K bath. Herein, however, the monitoring was performed with the catalyst sample in a quartz cell under a 295 K bath (Chart S2). In both sample setups, the metal sites absorbed UV and/or visible light, converting the light energy to heat, forming hot spots, as discussed for surface-enhanced Raman spectroscopy using probe molecules on Au−Ag/Ag_2S,[34] Au/TiO_2-poly(*N*-isopropylacrylamide),[35] the small gaps between Au and $W_{18}O_{49}$ on TiO_2[36] and between Au nanoparticles,[37] plasmon difference between Au nanoparticles and nanorods,[38] and theoretical analyses of photothermal heating of Au nanoparticle.[39]

The irradiated light intensity corresponded to 0.65 J s^{-1} for a 1 cm^2 sample. Therefore, the temperature increase was <12 K s^{-1} and <11 K s^{-1} for the Ru−Ni−ZrO_2 and Ni−ZrO_2 samples, respectively, based on the heat capacity of ZrO_2 (0.455 J g^{-1} K^{-1}), Ni (0.444 J g^{-1} K^{-1}), and Ru (0.238 J g^{-1} K^{-1})[3,16] in the absence of an EG bath, and >0.18 K min^{-1} based on the heat capacity of EG (2.394 J g^{-1} K^{-1})[16] when an EG bath was used. The observed temperature increase of Ni was >15 K min^{-1} (Figure 2A(4)). Thus, the system quickly reached a heat dissipation equilibrium at the Ni hot spot, where the light-induced heating was balanced by ZrO_2 (Figures S4−S6), the EXAFS quartz cell, and EG. Under the EG bath, the irradiated light intensity increased to 654 mW cm^{-2}, compared to 90 mW cm^{-2} without the bath; however, the resulting Ni temperature remained similar, 391−399 K (Table S1c,d). The temperature achieved was determined by the light intensity and the presence or absence of the 295 K EG bath and was independent of the heat capacities of the nanoparticle metals (Table S1).[16]

The conditions of the Ru−Ni−ZrO_2 sample during EXAFS σ monitoring closely resemble the photocatalytic test conditions using $^{13}CO_2$, H_2, and UV−visible light irradiation at 568 mW cm^{-2} under the 295 K bath (Figure 1)), suggesting that the Ni and Ru temperature monitored via the EXAFS σ factor (Figure 2A(4),B(4)) reflect the reactivity of multiple hydrogenation steps converting COH species, transferred from $V_O^{\bullet\bullet}$ sites on the ZrO_2 surface, into CH_4 based on kinetic results[4,5] and DFT calculations[27] (see Section 3.4; Section 3.1).

When UV−visible light was not irradiated at 295 K, the $^{13}CH_4$ formation rate was as low as 53 nmol h^{-1} g_{cat}^{-1} using Ni (10 wt %)−ZrO_2,[3] which is approximately 3 orders of magnitude lower than the rates of 21−26 μmol h^{-1} g_{cat}^{-1} using Ni (10 wt %)−ZrO_2 and Ru (1.0 wt %)−Ni (10 wt %)−ZrO_2 under 568 mW cm^{-2} light with a 295 K bath (Figure 1(1)), suggesting the contribution of charge separation in ZrO_2 and/or photothermal effects of local metal sites under light irradiation.

https://doi.org/10.1021/jacs.5c17533
J. Am. Chem. Soc. XXXX, XXX, XXX−XXX

The warming of the Ni site to 399 ± 29 K for Ru (1.0 wt %)−Ni (10 wt %)−ZrO_2 (Figure 2A(4)) is consistent with the proposed reaction pathway: CO_2 adsorption on $V_O^{\bullet\bullet}$ sites at the ZrO_2 surface, followed by the transfer of COH species to Ni or another metal nanoparticle surface, which is heated by light to 317−459 K, enabling multiple hydrogenation reactions (Table S1).[3−5,12,13,27]

3.3. Intermediate Monitoring via FTIR

The adsorbed species and reaction intermediates were monitored under $^{13}CO_2$, H_2, and UV−visible light irradiation. Using the Ni−ZrO_2 sample, negligible peaks appeared under $^{13}CO_2$ and H_2 at 295 K in the CO stretching region (Figure 3B1(a),(b)). Upon irradiation with UV−visible light (90 mW cm^{-2}) for 1 h, a weak, broad peak appeared at 2015 cm^{-1} (d), which was assigned to the ^{13}CO stretching vibration (ν(^{13}CO)) adsorbed on Ni atoms.[3] However, the peak did not grow well, even after 20 h of light irradiation (f). Intermittent noise grew in Figure 3B(a)−(e) was basically owing to photocatalytically, exothermically formed H_2O via eq S2, in accord with the intermittent noise also at 4000−3500 cm^{-1}.[40] The noise level varied due to the dew point at room temperature (Figure 3A,B).

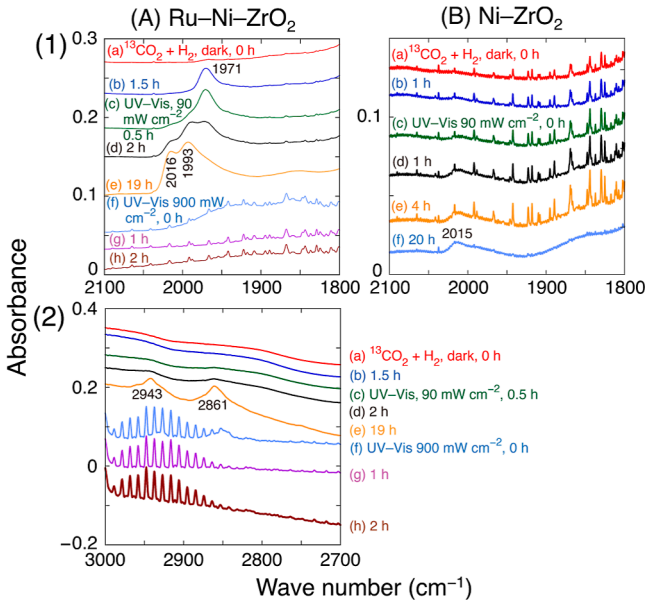

Figure 3. Time-course FTIR spectra: (1) CO stretching region: (A) Ru (1.0 wt %)−Ni (10 wt %)−ZrO_2-723R under $^{13}CO_2$ (2.3 kPa) and H_2 (21.7 kPa) at 0 h (a), 1.5 h (b) under dark, and 0.5 h (c), 2 h (d), and 19 h (e) under UV−visible irradiation (90 mW cm^{-2}), and 0 h (f), 1 h (g), and 2 h (h) under UV−visible irradiation (900 mW cm^{-2}). (B) Ni (10 wt %)−ZrO_2-723R (B) under $^{13}CO_2$ (2.3 kPa) and H_2 (21.7 kPa) at 0 h (a), 1 h (b) under dark, and 0 h (c), 1 h (d), 4 h (e), and 20 h (f) under UV−visible irradiation (90 mW cm^{-2}). (2) CH_x stretching region: Ru (1.0 wt %)−Ni (10 wt %)−ZrO_2-723R. Intermittent noise basically owing to photocatalytically formed H_2O[40] appeared in spectra A(f)−(h) and B(a)−(e).

By contrast, using the Ru−Ni−ZrO_2 photocatalyst, a broad peak appeared at 1971 cm^{-1} under $^{13}CO_2$ and H_2 even before UV−visible light irradiation (Figure 3A1(b)). Based on the following correlation

$$\tilde{\nu} = \frac{1}{2\pi c}\sqrt{\frac{k}{\mu}} \quad (3)$$

and

$$\frac{\tilde{\nu}_{13_{CO}}}{\tilde{\nu}_{12_{CO}}} = \frac{\sqrt{\frac{1}{13}+\frac{1}{16}}}{\sqrt{\frac{1}{12}+\frac{1}{16}}} = 0.97778 \quad (4)$$

where $\tilde{\nu}$ is the wavenumber, c is the speed of light, k is the force constant, and μ is the reduced mass of bonding atoms, the peak at 1971 cm^{-1} corresponds to the ν(^{12}CO) peak on Ni atoms originating from $^{12}CO_2$ adsorbed on $V_O^{\bullet\bullet}$ sites at the ZrO_2 surface (1585 and 1342 cm^{-1}; see Section 4, Figure S7A), compared to the ν(^{13}CO) peak at 2015 cm^{-1}. The ν(^{12}CO) peak intensity increased by 40% under UV−visible light irradiation (90 mW cm^{-2}) for 0.5 h (c). A new peak appeared at 1993 cm^{-1} as a shoulder after 2 h of light irradiation with a weak ν(^{13}CO) peak on Ni at 2016 cm^{-1} (d). After 19 h of light irradiation, the peaks at 2016 and 1993 cm^{-1} became the major features (e). The peak at 1993 cm^{-1} can be assigned to ν(^{13}CO) of ^{13}CO adsorbed on Ru atoms.

When the UV−visible light intensity irradiating the Ru−Ni−ZrO_2 photocatalyst increased from 90 to 900 mW cm^{-2} (Figure 3A1(f)−(h)), both ν(^{13}CO) peaks on Ni (2016 cm^{-1}) and Ru (1993 cm^{-1}) disappeared, likely owing to desorption and/or conversion to CH_4.

The transformation of surface species was also followed in the C−H stretching region using Ru−Ni−ZrO_2 (Figure 3A(2)). Under $^{13}CO_2$ and H_2, a pair of peaks slowly grew at 2943 and 2861 cm^{-1} over 2−19 h of UV−visible light irradiation (spectra d and e), corresponding to the antisymmetric ν(CH_{as}) and symmetric ν(CH_s) stretching vibrations of $^{13}CH_3$ species.[3]

By contrast, when the irradiation light intensity increased from 90 to 900 mW cm^{-2}, the pair of peaks corresponding to ν(CH_{as}) and ν(CH_s) quickly disappeared, and the P branch ($\Delta J = -1$) of ν_3 triplet stretching vibration of gaseous CH_4 catalytically formed appeared (spectra f−h). Together with the behavior of the ν(CO) peaks (Figure 3A(1)), this indicates that the ^{13}CO and $^{13}CH_3$ species on Ni and/or Ru either desorbed as CO and/or photoconverted to CH_4 owing to the effect of Ru.

The light intensity of 90 mW cm^{-2} was insufficient to fully activate the redox reactions over ZrO_2 via charge separation.[5] However, the specific role of Ru atoms on Ni nanoparticles was suggested: they facilitated the splitting of $^{12}CO_2$ transferred from the ZrO_2 surface to ^{12}CO and the splitting of $^{13}CO_2$ from the gas phase to ^{13}CO on either Ni or Ru (Figure 3A1(a)−(e)). These reaction steps are likely responsible for the promoted $^{13}CH_4$ formation observed with Ru−Ni−ZrO_2 compared to Ni−ZrO_2 (Figure 1A(2),B(2)). Under the high irradiation intensity of 900 mW cm^{-2}, the adsorption equilibrium of $^{13}CO_2$, its dissociation to ^{13}CO, and subsequent multiple hydrogenation on the Ru−Ni surface occurred rapidly enough to allow observation of the intermediate species leading to CH_4, consistent with the catalytic test results at 568 mW cm^{-2} without the 295 K bath (Figure 1A(2),B(2)).

3.4. Photocatalytic CO_2 Reduction Pathway

The pathway of photocatalytic CO_2 reduction over metallic Ni^0−ZrO_2 photocatalyst has been reported via CO_2 adsorption and one-electron reduction at the $V_O^{\bullet\bullet}$ sites on the ZrO_2 surface, followed by multiple hydrogenation steps of transferred COH and/or CO species over the Ni^0 surface, driven by heat generated from light energy absorbed by the Ni^0

https://doi.org/10.1021/jacs.5c17533
J. Am. Chem. Soc. XXXX, XXX, XXX−XXX

Scheme 1. Proposed Photocatalytic Reaction Pathway and Corresponding Free Energy Calculations for CO_2 Photoreduction to Proceed Over (A,B) Single Ru−Ni−ZrO_2 and (B′) Ni−ZrO_2 Photocatalysts[a]

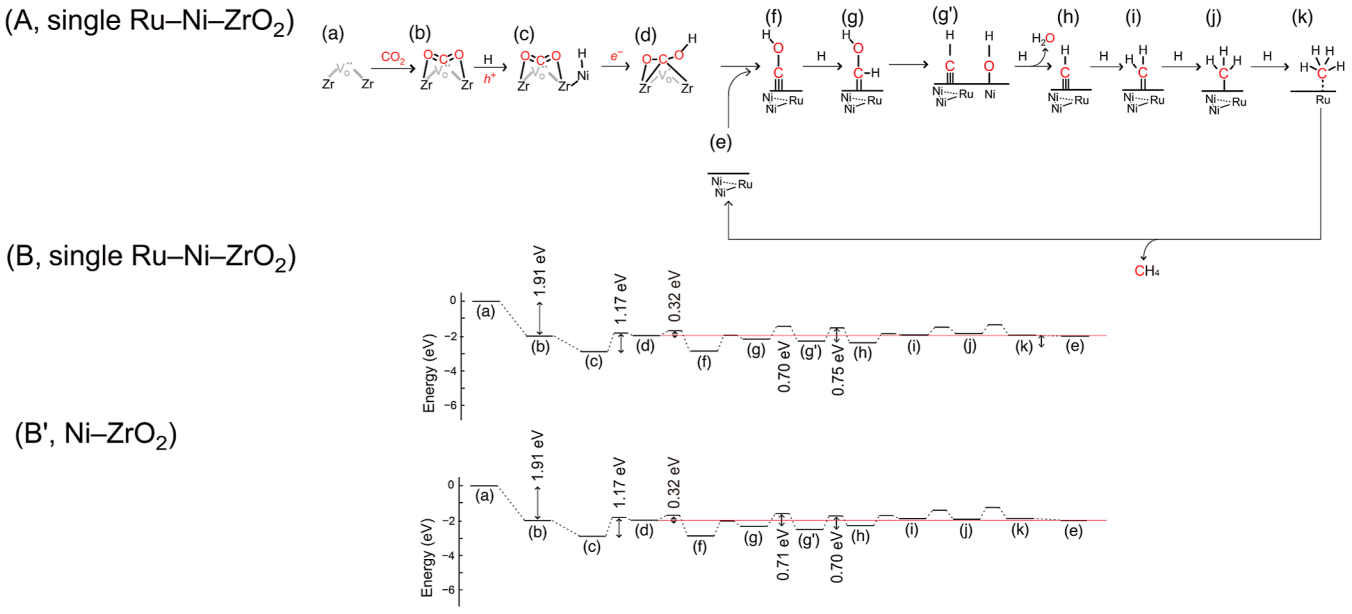

[a]For the Ni−ZrO_2 photocatalyst, the surface metallic sites are Ni_3 and Ni sites, rather than the Ni_2Ru and Ru sites illustrated in panel A.

nanoparticles,[27] as evidenced in this study (Figure 2(4)). The presence of $V_O^{\bullet\bullet}$ sites was confirmed based on the $^{13}CO_2$ exchange reaction with $^{12}CO_2$ adsorbed at $V_O^{\bullet\bullet}$ sites (Section 3.2) supported by DFT calculations with the CI-NEB method[27] (Scheme 1A(b),B′(b)).

The CO_2 adsorbed at $V_O^{\bullet\bullet}$ sites was suggested to hydrogenate to OCOH species, which was rate-determining with E_{act} = 1.17 eV (Schemes 1B′(c),(d)). The following dissociation step was facilitated at the $V_O^{\bullet\bullet}$ sites neighboring to Ni−Ru or Ni nanoparticle with E_{act} = 0.32 eV to COH species that was transferred to Ni−Ru or Ni surface leaving O atom at the $V_O^{\bullet\bullet}$ site, in comparison to $V_O^{\bullet\bullet}$ sites of ZrO_2 distant from Ni−Ru or Ni nanoparticle with E_{act} = 1.18−1.30 eV to COH or CO species.[27]

The following steps require lower E_{act} values than the rate-determining step on ZrO_2 from Schemes 1B′(c),(d). Among several possible COH hydrogenation pathways, the route from hydroxymethin (Schemes 1A(g),B′(g)) to methin (g′), followed by hydrogenative dehydration (h), was found to be the most favorable compared with other routes illustrated in Scheme S1 (Section 6.3).

Next, the CO_2 photoreduction route using the Ru (1.0 wt %)−Ni (10 wt %)−ZrO_2-723R photocatalyst was considered. A hemispherical $RuNi_{18}$ cluster exposing the Ni (1 1 1) surface was combined with the monoclinic ZrO_2 (1 1 1) surface (Scheme S2). The *N* value for surface Ni sites with a mean size of 1.6 nm (Figure S9A) is 8.0, while the observed *N* value for Ru−Ni was ∼4.1 (Figure S9). When a Ru adatom was structure-stabilized on the Ni (1 1 1) surface, the *R* value for Ru−Ni initially appeared unrealistically short (0.23 nm), demonstrating that a Ru atom replaced a Ni atom on the Ni (1 1 1) surface. The discrepancy in the *N* value for the Ru−Ni pair likely reflects that a minor portion of the impregnated Ru was oxidized, as suggested by the small positive shift of the Ru K-edge compared to metallic Ru (Figure 2B(1)). In fact, a Ni atom was substituted by a Ru atom at the Ni (1 1 1) surface, and the structure of the system was stabilized. The mean *R* for Ru−Ni (0.250 nm) after structure stabilization (Scheme S2(a)) was similar to that of Ru−Ni (0.240 nm) based on EXAFS curve-fit analysis (Figure S9A) and the Ni−Ni distance (0.24917 nm) in a metallic Ni crystal.[16] This surface site substitution model is in accord with previously reported Ru site models in the literature.[8−10]

The reduction pathway and energy diagram were compared between the $RuNi_{18}$ cluster exposing the (1 1 1) face and the Ni_{19} cluster exposing the (1 1 1) face, both combined with the ZrO_2 (1 1 1) surface. The pathways from CO_2 to CH_4 over the binary sites of ZrO_2 and the nanocluster of Ni and/or Ru atoms were very similar for both Ru−Ni−ZrO_2 and Ni−ZrO_2 (Schemes 1B,B′). The most favorable route shared a common E_{act} of 1.17 eV for the hydrogenation of adsorbed CO_2 at the $V_O^{\bullet\bullet}$ site (species c and d), followed by the second highest energy step, the hydrogenative hydration of methin from g′ to h, with an E_{act} of 0.75 eV over the single Ru−Ni sites, resembling 0.70 eV for the same step over Ni sites.

Thus, Ru exhibited no promotion effect in the photocatalytic route from CO_2 to CH_4, consistent with the negligible effect of Ru (19% decrease, Figure 1B(1)) observed in the photocatalytic reduction tests under a 295 K water bath. Across the entire pathway from CO_2 to CH_4, the hydrogenation of CO_2 adsorbed on $V_O^{\bullet\bullet}$ sites at the ZrO_2 surface to form OCOH species (Schemes 1A,B, and B′(c),(d)) required the highest E_{act} of 1.17 eV.

The observed molar fraction of $^{12}CH_4$ formation $\left(\frac{^{12}CH_4}{^{12}CH_4 + {}^{13}CH_4}\right)$ of 5.0 mol %−5.2 mol % (Figure 1B(1)), apparently greater than the 1 mol % $^{12}CO_2$ impurity in the $^{13}CO_2$ reagent, for both Ni−ZrO_2 and Ru−Ni−ZrO_2 photocatalysts, indicates the contribution of the ZrO_2 surface to photocatalysis via CO_2 adsorption and the subsequent reduction step via charge separation in ZrO_2 (Scheme 1).

https://doi.org/10.1021/jacs.5c17533
J. Am. Chem. Soc. XXXX, XXX, XXX−XXX

Scheme 2. (A) Proposed Thermal Reaction Pathway and Corresponding Free Energy Calculations for CO_2 Reduction Using (B) Ni−ZrO_2 and (B′) Single Ru−Ni−ZrO_2 Photocatalysts[a]

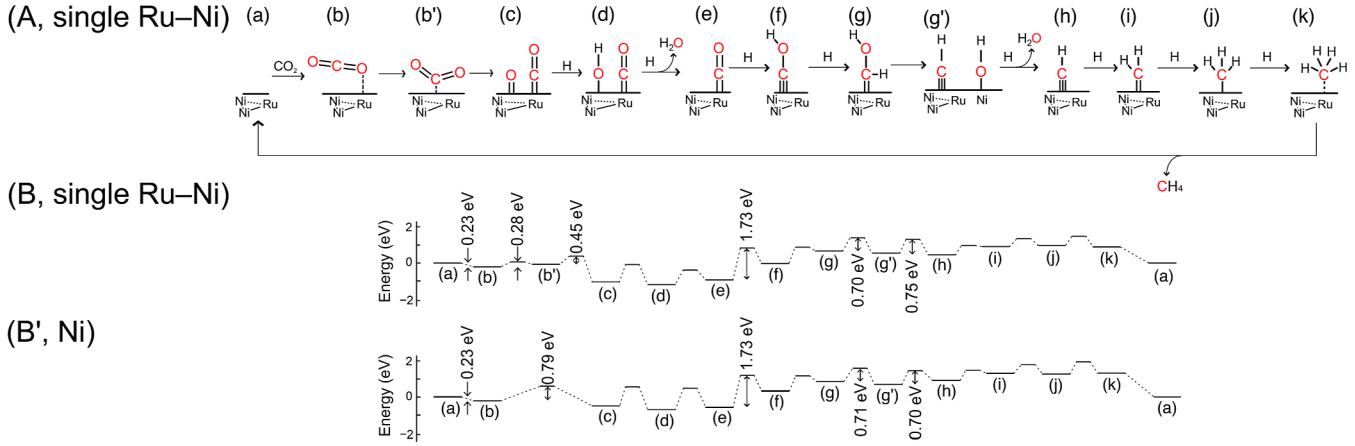

[a]For the Ni−ZrO_2 photocatalyst, the surface metallic sites are the Ni_3 and Ni sites, rather than the Ni_2Ru and Ru sites illustrated in panel A.

Scheme 3. Mechanistic Comparison of Photocatalytic (A) and Thermal CO_2 Reduction to CH_4 Converted From Light Energy (B)[a]

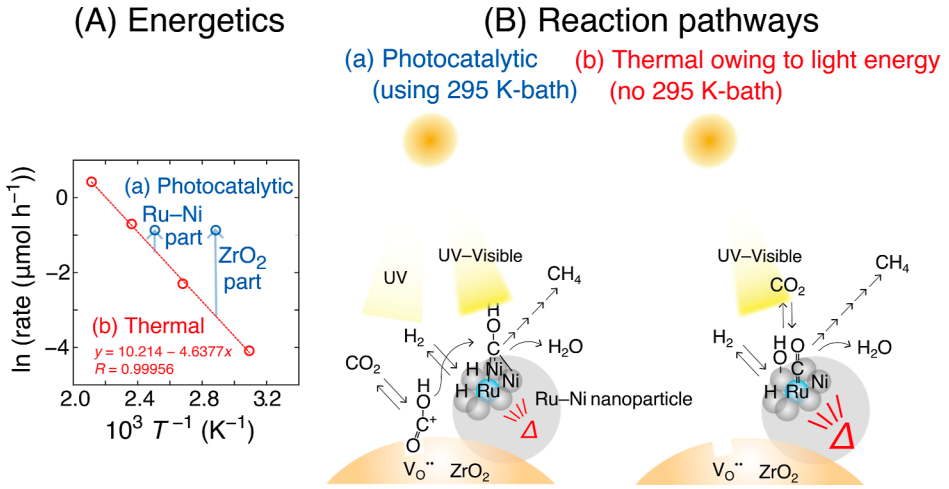

[a]Arrhenius plot for the reaction of CO_2 and H_2 using Ru (1.0 wt %) By contrast, CO_2Ni (10 wt %) By contrast, CO_2ZrO_2 at 323−473 K heated by heater is compared to the $^{13}CH_4$ formation rate in the photocatalytic reduction using $^{13}CO_2$, H_2, and Ru (1.0 wt %) By contrast, CO_2Ni (10 wt %) By contrast, CO_2ZrO_2 irradiated by UV−visible light (568 mW cm^{-2}) under a 295 K bath (Figure 1(1) and Chart S1). In the latter test, the Ni site temperature increased to 399 K (Figure 2B(4)), while the ZrO_2 site remained at 323 K.

3.5. Thermal CO_2 Reduction Pathway and the Effects of Ru

Finally, the pathway of thermal CO_2 reduction was evaluated, which is controlled exclusively by heat generated from light energy and is unaffected by charge separation in the semiconductor, owing to light irradiation. Under these catalytic conditions, the effects of single Ru atom substitution were evaluated based on DFT calculations with the CI-NEB method.

In thermal catalysis, the major role of ZrO_2 is to disperse Ni and/or Ru nanoparticles on the ZrO_2 surface, and the effect of its amphoteric nature and strong metal−support interaction is very limited. Thus, all steps along the pathway from CO_2 to CH_4 were assumed to occur on the Ni (1 1 1) surface, with one Ni atom substituted by a Ru atom (Schemes 2A and S3a).

The catalytic effect of a single Ru atom embedded in the metallic Ni surface was clearly identified in the adsorption stage of CO_2 (Schemes 2B,B′). CO_2 adsorbed on the Ru atom via an O atom (μ_1−OCO; Scheme 2A(b)) with an E_{ads} of −0.23 eV (Scheme 2B(b)) and was subsequently transformed to a 3-fold bridging adsorption via the C atom at the $RuNi_2$ site (μ_3-CO_2; Scheme 2A(b′)) with an E_{ads} value of −0.07 eV (Scheme 2B(b′)). By contrast, CO_2 adsorbed on a Ni atom via the O atom with an E_{ads} of −0.23 eV (Scheme 2B′(b)) did not convert to the μ-CO_2 state in the absence of a Ru atom. Similar promotional effects of CO_2 adsorption have been reported for single Ru atoms alloyed with Ni or Cu to enhance CO_2 reduction.[8−10]

The E_{act} value for μ_3-CO_2 dissociation into CO and O species was 0.45 eV on the Ni_2Ru site (Schemes 2A,B(b′),(c)) while the E_{act} value for μ_1-OCO to directly dissociating into CO and O species was significantly higher at 0.79 eV on the Ni_3 site (Scheme 2B′(b),(c)) mostly because the C═O moiety of the μ_1-OCO species could not effectively approach the Ni surface.

In the following steps from dissociated CO species to CH_4, the reaction pathways were essentially identical on the single

https://doi.org/10.1021/jacs.5c17533
J. Am. Chem. Soc. XXXX, XXX, XXX−XXX

Ru−Ni surface (Scheme 2B) and the Ni surface (Scheme 2B′), with the highest common E_{act} of 1.73 eV for the conversion of CO species to COH species at the Ni_2Ru (Scheme 2A,B(e), (f)) and Ni_3 sites (Scheme 2B′(e),(f)).

In summary, as the UV−visible light intensity increases, thermal effects on Ru−Ni dominate over redox reactions driven by charge separation in ZrO_2 induced by light. In the photothermal pathway, CO_2 is stabilized on sites associated with the Ru atom, facilitating its dissociation into CO, in clear contrast to pure Ni surfaces, where CO_2 stabilization is minimal. This kinetic difference clearly accounts for the >2.7× promotion of the CO_2 conversion rate into CH_4 by adding a Ru atom under UV−visible light irradiation at 568 mW cm^{-2} in the absence of a 295 K bath (Figure 1A(2)). The molar fraction of $^{12}CH_4$ formation ($\frac{12CH_4}{12CH_4 + 13CH_4}$) of 0.8 mol %−1.0 mol %, nearly matching the molar ratio of $^{12}CO_2$ (1.0 mol %) in $^{13}CO_2$ reagent, indicating that the ZrO_2 surface plays a negligible role in catalysis under these conditions and that $^{12}CO_2$ adsorbed at surface sites does not reach equilibrium with $^{13}CO_2$ during the reaction pathway, as depicted in Scheme 3B.

The critical difference between photocatalytic CO_2 reduction and thermal CO_2 reduction driven solely by light-induced heating is summarized in Scheme 3. The thermal reaction follows simple Arrhenius kinetics with an E_{act} value of 38.6 kJ mol^{-1} (Scheme 3A(b)), along the reaction pathway over the Ru−Ni surface (Scheme 2A). By contrast, for the photocatalytic reaction, the local temperature at the Ni site needs to be monitored using site-specific techniques,[3−5,12,13,32−37] which was measured at 399 K (@654 mW cm^{-2}, Figure 2A(4)). This accounts for a 1.72-fold promotion of CH_4 formation compared to the rate predicted by simple Arrhenius kinetics (Scheme 3A, arrow on the left). Meanwhile, the ZrO_2 sites reached 323 K @142 mW cm^{-2} (Figure S11) or 347 K @ 670 mW cm^{-2} (Figure S12A), corresponding to a 9.8-fold enhancement compared to the Arrhenius plot under the light irradiation of 670 mW cm^{-2} (Scheme 3A, arrow on the right). These results clearly demonstrate a combinational pathway in which initial CO_2 photoreduction occurs via charge separation in ZrO_2 as supported by the $^{12}CH_4$ ratio of 5.0 mol %−5.2 mol % (Figure 1(1)) and the substitution of $^{12}CO_2$-derived ^{12}CO by $^{13}CO_2$-derived ^{13}CO leading to CH_4 (Figure 3), followed by multiple hydrogenation steps on the Ni surface (Scheme 1A). As also discussed in cathodic CO_2 reduction pathways, further reduction of CO/COH intermediates to hydrocarbons often requires a metal surface,[41] presumably serving as a hot spot, similar to the Ni sites in this study.

4. CONCLUSIONS

The origin of the catalytic reaction for CO_2 reduction under UV−visible light irradiation was thoroughly investigated using Ru−Ni−ZrO_2 and Ni−ZrO_2 catalysts, based on kinetic tests conducted with or without a 295 K water bath, Ni and Ru K-edge EXAFS, FTIR, and DFT calculations with the CI-NEB method. Under UV−visible light irradiation at an intensity of 568 mW cm^{-2} in the absence of a 295 K bath, the CH_4 formation rate using the Ru−Ni−ZrO_2 catalyst was >2.7× higher than that using the Ni−ZrO_2 catalyst. This enhancement occurred because the reaction proceeded exclusively on the Ru−Ni or Ni surface owing to heat generated from light absorption. The dissociation of CO_2 into CO was the key promoted by the Ru atom, with E_{act} = 0.45 eV, compared to 0.79 eV on a pure Ni nanoparticle surface. By contrast, under UV−visible light irradiation at an intensity of 568 mW cm^{-2} with the quartz reactor maintained at 295 K, the Ni site behaved as a hot spot, as probed by the Debye−Waller factor, reaching 399 ± 29 K under CO_2, H_2, and UV−visible light irradiation. This hot spot did not mean simple photothermal catalysis in the absence of the 295 K bath; the CH_4 formation rate on Ni at 399 K, in thermal equilibrium with ZrO_2, the reactor, and H_2O/EG under the 295 K bath, was 1.72 times higher than the rate predicted by a simple photothermal reaction at 399 K. This demonstrates the combined effect of local heating and the reduction of CO_2 to COH at the $V_O^{\bullet\bullet}$ site as supported by DFT calculations via charge separation in ZrO_2 induced by UV and/or visible light irradiation.

■ ASSOCIATED CONTENT

Supporting Information

The Supporting Information is available free of charge at https://pubs.acs.org/doi/10.1021/jacs.5c17533.

Novelty claim, irradiated light wavelength distribution and intensity, experimental setups, UV−visible, XRD, HR-TEM, FTIR, correlated Debye model information and EXAFS data, photocatalytic CO_2 reduction rate dependence on Ru content, $^{13}CO_2$ photoexchange, and detailed pathway of CO_2 reduction and the three-dimensional illustration based on DFT calculations (DOCX)

■ AUTHOR INFORMATION

Corresponding Authors

Hongwei Zhang − *Key Laboratory of Development and Application of Rural Renewable Energy, Biogas Institute of Ministry of Agriculture and Rural Affairs, Chengdu 610041, People's Republic of China;* orcid.org/0000-0002-6773-8769; Email: zhw9590@163.com

Yasuo Izumi − *Department of Chemistry, Graduate School of Science, Chiba University, Inage-ku, Chiba 263-8522, Japan;* orcid.org/0000-0001-8366-1864; Email: yizumi@faculty.chiba-u.jp

Authors

Masahito Sasaki − *Department of Chemistry, Graduate School of Science, Chiba University, Inage-ku, Chiba 263-8522, Japan*

Tomoki Oyumi − *Department of Chemistry, Graduate School of Science, Chiba University, Inage-ku, Chiba 263-8522, Japan*

Keisuke Hara − *Department of Chemistry, Graduate School of Science, Chiba University, Inage-ku, Chiba 263-8522, Japan*

Complete contact information is available at: https://pubs.acs.org/10.1021/jacs.5c17533

Notes

The authors declare no competing financial interest.

■ ACKNOWLEDGMENTS

The authors are grateful for the financial support from the Grant-in-Aid for Scientific Research B (24K01522, 20H02834, Y.I.) from the Japan Society for the Promotion of Science. X-ray absorption experiments were performed with the approval of the Photon Factory Proposal Review Committee

(2022G527, 2021G546, 2020G676, and 2019G141). A part of the computation was performed using the facilities of the Institute for Solid State Physics, University of Tokyo (2025-Bb-0019 and 2024-Bb-0004). The authors would like to thank Ikki Abe and Dr. Xiaolei Guo for experimental support and Enago (www.enago.jp) for the language review.

REFERENCES

(1) Izumi, Y. Recent Advances in the Photocatalytic Conversion of Carbon Dioxide to Fuels with Water and/or Hydrogen Using Solar Energy and Beyond. *Coord. Chem. Rev.* **2013**, *257*, 171−186.

(2) Izumi, Y. *ACS Books "Advances in CO_2 Capture, Sequestration, and Conversion"*, Jin, F.; He, L.-N.; Hu, Y. H., Eds., *ACS Symposium Series*; ACS Publications, 2015; Vol. *1194*, Chapter 1, pp 1−46.

(3) Zhang, H.; Itoi, T.; Konishi, T.; Izumi, Y. Efficient and Selective Interplay Revealed: CO_2 Reduction to CO over ZrO_2 by Light with Further Reduction to Methane over Ni^0 by Heat Converted from Light. *Angew. Chem., Int. Ed.* **2021**, *60*, 9045−9054.

(4) Loumissi, T.; Ishii, R.; Hara, K.; Oyumi, T.; Abe, I.; Li, C.; Zhang, H.; Hirayama, R.; Niki, K.; Itoi, T.; Izumi, Y. Exchange of CO_2 with CO as Reactant Switches Selectivity in Photoreduction on Co−ZrO_2 from C_{1-3} Paraffins to Small Olefins. *Angew. Chem., Int. Ed.* **2024**, *63*, No. e202412090.

(5) Oyumi, T.; Abe, I.; Sasaki, M.; Izumi, Y. Light Intensity-Directed Selective CO_2 Photoreduction Using Iron(0)−Zirconium Dioxide Photocatalyst. *Chem. Commun.* **2025**, *61*, 8671−8674.

(6) Thampi, K. R.; Kiwi, J.; Grätzel, M. Methanation and Photo-Methanation of Carbon Dioxide at Room Temperature and Atmospheric Pressure. *Nature* **1987**, *327*, 506−508.

(7) Melsheimer, J.; Guo, W.; Ziegler, D.; Wesemann, M.; Schlögl, R. Methanation of Carbon Dioxide over Ru/Titania at Room Temperature: Explorations for a Photoassisted Catalytic Reaction. *Catal. Lett.* **1991**, *11*, 157−168.

(8) Zhang, T.; Zheng, P.; Gao, J.; Han, Z.; Gu, F.; Xu, W.; Li, L.; Zhu, T.; Zhong, Z.; Xu, G.; et al. Single-Atom Ru Alloyed with Ni Nanoparticles Boosts CO_2 Methanation. *Small* **2024**, *20*, 2308193.

(9) Zhang, T.; Zheng, P.; Gu, F.; Xu, W.; Chen, W.; Zhu, T.; Han, Y.-F.; Xu, G.; Zhong, Z.; Su, F. The Dual-Active-Site Tandem Catalyst Containing Ru Single Atoms and Ni Nanoparticles Boosts CO_2 Methanation. *Appl. Catal., B* **2023**, *323*, 122190.

(10) Liu, L.; Hu, J.; Sheng, Y.; Akhoundzadeh, H.; Tu, W.; Siow, W. J. S.; Ong, J. H.; Huang, H.; Xu, R. Ru Single Atom Dispersed Cu Nanoparticle with Dual Sites Enables Outstanding Photocatalytic CO_2 Reduction. *ACS Nano* **2024**, *18*, 26271−26280.

(11) Liu, C.; Tang, S.; Song, R.; Xu, Y.-F.; Ozin, G. A.; Yao, X. Micro/Nanoscale Thermometry in Photothermal Catalysis. *Joule* **2025**, *9* (8), 102052.

(12) Zhang, H.; Itoi, T.; Konishi, T.; Izumi, Y. Dual Photocatalytic Roles of Light: Charge Separation at the Band Gap and Heat via Localized Surface Plasmon Resonance To Convert CO_2 into CO over Silver−Zirconium Oxide. *J. Am. Chem. Soc.* **2019**, *141*, 6292−6301.

(13) Zhang, H.; Itoi, R.; Niki, K.; Konishi, T.; Izumi, Y. Dual Origins of Photocatalysis: Light-Induced Band-Gap Excitation of Zirconium Oxide and Ambient Heat Activation of Gold to Enable $^{13}CO_2$ Photoreduction/Conversion. *Catal. Today* **2020**, *356*, 544−556.

(14) Bearden, J. A. X-Ray Wavelengths. *Rev. Mod. Phys.* **1967**, *39*, 78−124.

(15) Vaarkamp, M.; Linders, H.; Koningsberger, D. *XDAP Version 3.2.9*; XAFS Services International: Woudenberg, The Netherlands, 2022.

(16) Haynes, W. M., Ed.; *CRC Handbook of Chemistry and Physics*, 96th ed.; CRC Press: Boca Raton, 2015; p 4−124, 12−216, 15−17 (C_p); 4−150, 12−17 (lattice constant).

(17) Groppo, E.; Prestipino, C.; Lamberti, C.; Carbpmo, R.; Boscherini, F.; Luches, P.; Valeri, S.; D'Addato, S. O K-edge X-Ray Absorption Study of Ultrathin NiO Epilayers Deposited In Situ on Ag (0 0 1). *Phys. Rev. B* **2004**, *70*, 1654081−1654086.

(18) Beni, G.; Platzman, P. M. Temperature and Polarization Dependence of Extended X-Ray Absorption Fine-Structure Spectra. *Phys. Rev. B:* **1976**, *14*, 1514−1518.

(19) Sevillano, E.; Meuth, H.; Rehr, J. J. Extended X-Ray Absorption Fine Structure Debye−Waller Factors. I. Monoatomic Crystals. *Phys. Rev. B* **1979**, *20*, 4908−4911.

(20) Gray, D. E., Ed.; *American Institute of Physics Handbook*, 3rd ed.;.McGraw-Hill: New York, 1972; pp 4−116.

(21) *Springer Handbook of Condensed Matter and Materials Data*; Martienssen, W., Warlimont, H., Eds.; Springer: Heidelberg, 2005; p 1014.

(22) Ankudinov, L.; Ravel, B.; Rehr, J. J.; Conradson, S. D. Real-Space Multiple-Scattering Calculation and Interpretation of X-Ray-Absorption Near-Edge Structure. *Phys. Rev. B Condens. Matter Mater. Phys.* **1998**, *58*, 7565−7576.

(23) Kresse, G.; Furthmüller, J. Efficient Iterative Schemes for *ab initio* Total-Energy Calculations Using a Plane-Wave Basis Set. *Phys. Rev. B* **1996**, *54*, 11169−11186.

(24) Hubbard, J. Electron Correlations in Narrow Energy Bands. *Proc. Royal Soc. A* **1963**, *276* (1365), 238−257.

(25) Anisimov, V. I.; Zaanen, J.; Andersen, O. K. Band Theory and Mott Insulators: Hubbard *U* Instead of Stoner *I*. *Phys. Rev. B* **1991**, *44* (3), 943−954.

(26) Henkelman, G.; Jonsson, H. Improved Tangent Estimate in the Nudged Elastic Band Method for Finding Minimum Energy Paths and Saddle Points. *J. Chem. Phys.* **2000**, *113*, 9978−9985.

(27) Hara, K.; Nozaki, M.; Hirayama, T.; Ishii, R.; Niki, K.; Izumi, Y. Adsorbed CO_2-Mediated CO_2 Photoconversion Cycle into Solar Fuel at the O Vacancy Site of Zirconium Oxide. *J. Phys. Chem. C* **2023**, *127*, 1776−1788.

(28) Kip, B. J.; Duivenvoorden, F. B. M.; Koningsberger, D. C.; Prins, R. Determination of Metal Particle Size of Highly Dispersed Rh, Ir, and Pt Catalysts by Hydrogen Chemisorption and EXAFS. *J. Catal.* **1987**, *105*, 26−38.

(29) Stohr, J. *NEXAFS Spectroscopy*; Springer: New York, 1992; p 13.

(30) Hoffmann, M. R.; Martin, S. T.; Choi, W.; Bahnemann, D. W. Environmental Applications of Semiconductor Photocatalysis. *Chem. Rev.* **1995**, *95*, 69−96.

(31) Liu, W.; Feng, H.; Yang, Y.; Niu, Y.; Wang, L.; Yin, P.; Hong, S.; Zhang, B.; Zhang, X.; Wei, M. Highly-Efficient RuNi Single Atom Alloy Catalysts Toward Chemoselective Hydrogenation of Nitroarenes. *Nat. Commun.* **2022**, *13*, 3188.

(32) Timoshenko, J.; Ahmadi, M.; Roldan Cuenya, B. Is There a Negative Thermal Expansion in Supported Metal Nanoparticles? An In Situ X-ray Absorption Study Coupled with Neural Network Analysis. *J. Phys. Chem. C* **2019**, *123* (33), 20594−20604.

(33) Vasina, T.; Bernard, J.; Benoit, M.; Calvo, F. Debye temperature of iron nanoparticles: Finite-size effects in the scaling regime. *Phys. Rev. B* **2022**, *105*, 245406.

(34) Wang, Q.-Y.; Chen, Y.-Y.; Ye, R.-K.; Liu, Q.; Chen, H.-Y.; Yang, H.; Li, M.-Y.; Hu, J.-Q.; Fang, P.-P. Instantly Detecting Catalysts' Hot Spots Temperature In Situ during Photocatalysis by Operando Raman Spectroscopy. *Anal. Chem.* **2021**, *93* (46), 15517−15524.

(35) Negrin−Montecelo, Y.; Comesaña−Hermo, M.; Kong, X.-T.; Rodorígues−González, B.; Wang, Z.; Pérez−Lorenzo, M.; Govorov, A. O.; Correa−Duarte, M. A. Traveling Hot Spots in Plasmonic Photocatalysis. Manipulating Interparticle Spacing for Real-Time Control of Electron Injection. *ChemCatChem* **2018**, *10* (7), 1561−1565.

(36) Jiang, X.; Huang, J.; Bi, Z.; Ni, W.; Gurzadyan, G.; Zhu, Y.; Zhang, Z. Plasmonic Active "Hot Spots"-Confined Photoctalytic CO_2 Reduction with High Selectivity for CH_4 Production. *Adv. Mater.* **2022**, *34* (14), 2109330.

(37) Wy, Y.; Jung, H.; Hong, J. W.; Han, S. W. Exploiting Plasmonic Hot Spots in Au-Based Nanostructures for Sensing and Photocatalysis. *Acc. Chem. Res.* **2022**, *55* (6), 831−842.

(38) Sousa−Castillo, A.; Comesaña−Hermo, M.; Rodriguez−González, B.; Pérez−Lorenzo, M.; Wang, Z.; Kong, X.-T.; Govorov,

https://doi.org/10.1021/jacs.5c17533
J. Am. Chem. Soc. XXXX, XXX, XXX−XXX

A. O.; Correa−Duarte, M. A. Boosting Hot Electron-Driven Photocatalysis through Anisotropic Plasmonic Nanoparticles with Hot Spots in Au−TiO_2 Nanoarchitectures. *J. Phys. Chem. C* **2016**, *120* (21), 11690−11699.
(39) Mascaretti, L.; Naldoni, A. Hot Electron and Thermal Effects in Plasmonic Photocatalysis. *J. Appl. Phys.* **2020**, *128* (4), 041101.
(40) Shimadzu Co. https://www.shimadzu.com/an/service-support/technical-support/ftir/faq/noise.html (checked on February 8, 2026).
(41) Nitopi, S.; Bertheussen, E.; Scott, S. B.; Liu, X.; Engstfeld, A. K.; Horch, S.; Seger, B.; Stephens, I. E. L.; Chan, K.; Hahn, C.; Nørskov, J. K.; Jaramillo, T.; Chorkendorff, I. Progress and Perspectives of Electrochemical CO_2 Reduction on Copper in Aqueous Electrolyte. *Chem. Rev.* **2019**, *119* (12), 7610−7672.

https://doi.org/10.1021/jacs.5c17533
J. Am. Chem. Soc. XXXX, XXX, XXX−XXX